Journal of Marine Research, 47, 457–492, 1989

Journal of
MARINE RESEARCH

Volume 47, Number 3

Wind-driven ocean circulation and equilibrium statistical mechanics

by Annalisa Griffa[1,2] and Rick Salmon[1]

ABSTRACT

In this paper, we show that numerical solutions of the single-layer quasigeostrophic equation in a beta-plane basin approach the state predicted by equilibrium statistical mechanics when the forcing and dissipation are (unrealistically) zero. This equilibrium state, which we call *Fofonoff flow*, consists of a quasi-steady uniform westward interior flow closed by inertial boundary layers. When wind stress and bottom drag are switched on, we find that the nonlinear terms in the quasigeostrophic equation still try to drive the flow toward Fofonoff flow, but their success at this depends strongly on the *geometry* of the wind stress. If the prescribed wind stress exerts a torque with the right sign to balance the bottom-drag torque around every closed streamline of the Fofonoff flow, then solutions to the *wind-driven* quasigeostrophic equation are energetic, Fofonoff-like, and nearly steady. If, on the other hand, the wind opposes Fofonoff flow, the wind-driven solutions are turbulent, with small mean flows, and much less energy. Our results suggest that integral conservation laws (on which the equilibrium statistical mechanics is solely based) largely define the role of the nonlinearities in the quasigeostrophic equation. To support this viewpoint, we demonstrate a resemblance between the solutions of the quasigeostrophic equation and the solutions of a stochastic model equation. The stochastic model equation, in which the advected vorticity is replaced by a random variable, has only gross conservation laws in common with the quasigeostrophic equation.

1. Introduction

Equilibrium statistical mechanics predicts that numerical solutions of the equation

$$\nabla^2\psi_t + J(\psi, \nabla^2\psi) + \beta\psi_x = \textit{wind curl} + \textit{friction} \qquad (1.1)$$

1. Scripps Institution of Oceanography, Mail Code A-025, La Jolla, California, 92093, U.S.A.
2. Present address: Rosenstiel School of Marine and Atmospheric Science, University of Miami, Miami, Florida, 33149, U.S.A.

for a single-layer quasigeostrophic ocean approach a *thermal equilibrium* state when the right-hand side of (1.1) is (unrealistically) zero. (Here, ψ is the streamfunction for the flow and the other symbols have their conventional meanings, defined fully below.) These thermal equilibrium states (e.g. Salmon *et al.*, 1976) are characterized by a mean flow $\langle\psi\rangle$ that satisfies

$$\nabla^2\langle\psi\rangle + \beta(y - y_0) = \gamma\langle\psi\rangle, \tag{1.2}$$

where y_0 and γ are constants determined by the initial energy, total potential vorticity, and potential enstrophy. For realistically small initial energy, γ is positive, and solutions of (1.2) have a constant westward interior flow closed by inertial boundary layers at the coasts, similar to Figure 5a. We call such mean flows *Fofonoff flows* after Fofonoff (1954). The thermal equilibrium states also contain time-dependent motions, but these are confined to relatively small spatial scales.

This paper assesses the relevance of thermal equilibrium theory to models with realistic forcing and friction by examining square-basin numerical solutions of (1.1) with a variety of wind-stress patterns. Section 2 provides the theoretical background. In Section 3 we confirm that unforced, undamped solutions of (1.1) do indeed approach solutions of (1.2). Section 4 examines solutions of (1.1) with realistic forcing and damping.

We find that when wind stress and friction are switched on, the nonlinear terms in (1.1) still try to drive the solution toward a quasi-steady Fofonoff state, but their success at this depends strongly on the *geometry* of the wind stress, as the following simple argument anticipates. Let

$$W = \iint \tau \cdot \mathbf{u}\, dx\, dy \tag{1.3}$$

where $\mathbf{u} = (-\psi_y, \psi_x)$ is the fluid velocity and τ is the wind stress. If $W > 0$, then the wind does work on the flow. However, the geometry of τ may be such that W cannot be positive for mean states resembling Fofonoff flows. For example, the wind might be westerly over the whole interior ocean and zero near latitudinal boundaries. Then quasi-steady Fofonoff flow is clearly impossible.

In Section 4, we consider the question of compatability between a given wind stress and Fofonoff flow more carefully, using the time-averaged integral of (1.1) over the area enclosed by a mean streamline of the flow. Then Fofonoff flow is possible only where the wind exerts a torque of the correct sign to balance the bottom-drag torque on Fofonoff flow *with no need for a Reynolds flux of potential vorticity*.

Our experiments show that, in cases and in regions where Fofonoff flow is possible by the foregoing criteria, the solutions of (1.1) are energetic, Fofonoff-like, and nearly steady, as anticipated by equilibrium statistical mechanics. When, on the other hand, the wind opposes Fofonoff flow, the solutions are turbulent, with small mean flows and much less total energy. In summary, the nonlinear terms in (1.1) always try to move the system toward quasi-steady Fofonoff flow. If the wind cooperates, they partly

succeed. However, if the wind opposes Fofonoff flow, then the system exhibits large fluctuations about a very weak mean flow.

Thermal equilibrium (and Fofonoff mean flows in particular) corresponds to a uniform probability distribution of system states over hypersurfaces in phase space corresponding to fixed values of the energy, total potential vorticity, and potential enstrophy. Our thesis that the nonlinear terms in (1.1) always push the system toward thermal equilibrium is thus equivalent to the principle that nonlinearities mix *probability density* over the accessible volume of *phase space*. This is distinct from the principle of *potential vorticity* mixing in *physical space*, which, unless selectively applied, grossly violates energy conservation.

If our thesis is correct, then quite different physical systems with the same gross conservation laws ought to behave similarly in the strongly nonlinear regime. In Section 5 we test this idea by comparing solutions of (1.1) to solutions of the stochastic model equation

$$\nabla^2\psi_t + J(\psi, \nabla^2\psi^*) + \beta\psi_x = \textit{wind curl} + \textit{friction} \tag{1.4}$$

where ψ^* is a random variable with only gross statistical properties in common with ψ. The only rigid constraint on ψ^* is that the Jacobian term in (1.4) not be a source of potential enstrophy. (The energy and total vorticity are automatically conserved by (1.4) when the right-hand side is zero.)

We find that time-averages of the solutions to (1.4) bear a surprising resemblance to those of (1.1). This suggests that fundamental properties of the solutions to (1.1) are *generic*, and that it is pointless to seek specific "mechanisms" for every observed property of nonlinear flow models.

The model (1.1) has been the subject of many previous papers. Veronis (1966) was the first to note that solutions of (1.1) can resemble Fofonoff flow. Niiler (1966) proposed an analytical explanation for this resemblance for the case of small wind curl and friction, but for the reasons stated above, his theory applies only to prescribed winds that can do positive work on Fofonoff flow. Marshall and Nurser (1986) present a similar theory for a baroclinic quasigeostrophic model. Merkine *et al.* (1985) have recently expressed doubt that Fofonoff flow has relevance to solutions of (1.1). We disagree with their conclusions for the reasons stated by Holloway (1986b).

The present paper, which is an incomplete summary of Griffa (1988), is our attempt at a qualitative synthesis of the solutions to (1.1). Our synthesis is based upon thermal equilibrium theory even in the cases where the solutions do not resemble Fofonoff flow. However, many of our experiments closely resemble numerical solutions that have appeared in the literature. See especially Marshall (1984).

2. Background

The quasigeostrophic equation for a single-layer ocean in a square basin is

$$\frac{\partial q}{\partial t} + J(\psi, q) = \left(\frac{\tau_0}{\rho H}\right) \operatorname{curl} \tau + D \tag{2.1}$$

where (x, y) are Cartesian coordinates in the (east, north) direction, $\psi(x, y, t)$ is the streamfunction, and the potential vorticity

$$q = \zeta + f \tag{2.2}$$

is the sum of the relative vorticity

$$\zeta = \nabla^2\psi \tag{2.3}$$

and the Coriolis parameter

$$f = f_0 + \beta y. \tag{2.4}$$

Here

$$J(A, B) = \frac{\partial A}{\partial x}\frac{\partial B}{\partial y} - \frac{\partial B}{\partial x}\frac{\partial A}{\partial y}, \tag{2.5}$$

ρ is the mass density, H is the constant depth, τ_0 is a representative wind stress magnitude, $\tau(x, y)$ is the wind stress (divided by τ_0), and D is a general dissipation operator discussed further below. The boundary conditions are $\psi = 0$ at the coastal boundaries.

The methods of equilibrium statistical mechanics predict the final states toward which finite-resolution models of macroscopic fluid systems would evolve in the absence of external forcing and viscosity. These thermal equilibrium states anticipate the role of fluid self-interactions in realistic, nonconservative flows. For a review of the theory and its previous applications to geophysical fluid dynamics, see Kraichnan and Montgomery (1980), Salmon (1982a, b), and Holloway (1986a). In this paper, we are primarily interested in assessing the relevance of thermal equilibrium theory to numerical solutions of (2.1) with realistic forcing and damping.

When $\tau = D = 0$, the dynamics (2.1) conserves the energy

$$E \equiv \iint_A (\nabla\psi)^2 \, dx \, dy \tag{2.6}$$

and the potential vorticity q on every fluid particle. (Here

$$\iint_A dx \, dy$$

denotes an integration over the whole basin.) It follows that every moment,

$$Q_n \equiv \iint_A q^n \, dx \, dy, \qquad n = 1, 2, \ldots \tag{2.7}$$

is also conserved.

Now suppose that (2.1) is replaced by a discrete numerical analogue,

$$\frac{d\psi_i(t)}{dt} = G_i(\psi_1, \psi_2, \ldots, \psi_N), \qquad i = 1 \text{ to } N \tag{2.8}$$

where $\psi_i(t)$ is the streamfunction at the i-th gridpoint or mode. If (as is generally the case) (2.8) statisfies the Liouville property,

$$\sum_{i=1}^{N} \frac{\partial G_i}{\partial \psi_i} = 0 \qquad \text{when} \qquad \tau = D = 0, \tag{2.9}$$

then equilibrium statistical mechanics predicts that ensembles of *free* (i.e. unforced and undamped) solutions of (2.8) approach the stationary equilibrium state with (macrocanonical) probability density

$$P(\psi_1, \psi_2, \ldots, \psi_N) = const \cdot \exp\left\{-\lambda_0 E - \sum_{j=1}^{\infty} \lambda_j Q_j\right\}. \tag{2.10}$$

Here E and Q_j are the conserved discrete analogues of (2.6) and (2.7), and the constants λ_j are determined by the average initial values of E and Q_j.

If moments Q_n with $n > 3$ are ignored, then the probability density

$$P(\psi_1, \psi_2, \ldots, \psi_N) = const \cdot \exp\{-\lambda_0 E - \lambda_1 Q_1 - \lambda_2 Q_2\} \tag{2.11}$$

depends only on the energy E, the total potential vorticity Q_1, and the potential enstrophy Q_2. (We come back to this step below.) A straightforward calculation (e.g. Salmon, 1982a, Section 5) then establishes that the average streamfunction,

$$\langle \psi_i \rangle = \iiint \ldots \int d\psi_1 \, d\psi_2 \ldots d\psi_N \, \psi_i \, P(\psi_1, \psi_2, \ldots, \psi_N) \tag{2.12}$$

obeys the discrete analogue of

$$\nabla^2 \langle \psi \rangle + \beta(y - y_0) = \gamma \langle \psi \rangle \tag{2.13}$$

where

$$\beta y_0 = -f_0 - \frac{\lambda_1}{2\lambda_2} \qquad \text{and} \qquad \gamma = \frac{\lambda_0}{\lambda_2}. \tag{2.14}$$

The relevance of thermal equilibrium ensembles with probability density (2.11) to solutions of (2.1) with realistic forcing and damping has always been questioned, and it is the central focus of this paper. The truncation of $\psi(x, y, t)$ to a finitie number of discrete variables $\psi_i(t)$, corresponding to a finite grid-spacing Δx or a maximum wavenumber k_{max}, is especially unrealistic in the limit of zero (eddy) viscosity. The usual argument considers the sequence of equilibrium states (for given average E, Q_1, and Q_2) as $k_{max} \to \infty$, and posits that this sequence of states *qualitatively* resembles the states exhibited by the freely evolving *continuum* system, in which $k_{max} = \infty$ from the start.

Carnevale and Frederiksen (1987) have carefully examined the dependence of the thermal equilibrium states on k_{max}. They show that, as $k_{max} \to \infty$, all of the energy ends up in the steady Fofonoff flow defined by (2.13) with the constants γ and y_0 then solely

determined by the initial energy and total vorticity,

$$Z \equiv \iint \zeta \, dx \, dy = Q_1 + \text{constant.} \tag{2.15}$$

A finite enstrophy is contained in time-dependent motions at infinite wavenumbers, but there are no transient motions at any *finite* wavenumber. Carnevale and Frederiksen further show that γ is always larger than $-k_{min}^2$, where k_{min} is the lowest wavenumber in the basin, and that the steady Fofonoff flow is therefore stable by Arnold's nonlinear stability criterion. As they point out, the stability of Fofonoff flow with $\gamma > -k_{min}^2$ is required for consistency of the statistical theory because the thermal equilibrium flow is asymptotically steady. The "negative temperature" thermal equilibrium states with $-k_{min}^2 < \gamma < 0$ correspond to initial conditions with unrealistically large energy (large Rossby number).

The asymptotically exact results of Carnevale and Frederiksen can be anticipated by the following more intuitive arguments. First consider *free* (i.e. unforced and undamped) *three-dimensional* turbulence governed by the Euler equations. In three-dimensional turbulence, the only important integral invariant is the energy, and the thermal equilibrium state has energy equipartition among Fourier modes at all wavenumbers less than k_{max}.

Next consider free *two-dimensional* turbulence, governed by (2.1–3) with $f = 0 = \tau = D$. For this case, energy equipartition is prevented by the requirement that the enstrophy

$$Z_2 \equiv \iint_A \zeta^2 \, dx \, dy \tag{2.16}$$

also be conserved. As shown by Kraichnan (1975), the constraint that (2.16) remain constant actually traps all of the energy at k_{min} as $k_{max} \to \infty$.

The case of freely evolving ($\tau = D = 0$) beta-plane flow governed by (2.1–4) is, in a sense, intermediate between two- and three-dimensional turbulence. In this case, the energy can spread to high wavenumbers, increasing the enstrophy Z_2, provided only that the potential enstrophy

$$\iint_A q^2 \, dx \, dy = Z_2 + 2 \iint_A \zeta \beta y \, dx \, dy + \text{constants} \tag{2.17}$$

remains constant. This requires that

$$-C \equiv \iint_A \zeta \beta y \, dx \, dy \tag{2.18}$$

decrease to offset the increase in Z_2. Thus the tendency for energy to equipartition among spatial Fourier modes forces a negative correlation between relative vorticity and latitude. This negative correlation between vorticity and latitude is a characteristic property of Fofonoff flow.

In numerical experiments, k_{max} is fixed at a relatively small value, and the pile up of

energy at k_{max} arrests the evolution toward the Fofonoff state. If k_{max} could be increased, this energy would spread into even higher wavenumbers, further increasing the enstrophy Z_2 and the anticorrelation C between vorticity and latitude, and thus causing a stronger mean Fofonoff flow. In numerical experiments, it is often impractical to increase k_{max}, but the energy piling up at k_{max} can be removed by a scale-selective eddy viscosity. Thus solutions of (2.1–4) in which τ vanishes and D represents only an eddy viscosity should exhibit the same strong Fofonoff flow as solutions with $\tau = D = 0$ and a much larger k_{max}. Such solutions are examined in Section 3.

As already stated, equilibrium statistical mechanics predicts that most of the energy in *time-dependent* motions is concentrated near k_{max}. A scale-selective eddy viscosity removes this time-dependent energy, thereby reducing the dimension of the volume in phase space available to the system. Thus, for the dynamics (2.1–4) with vanishing τ and D only an eddy viscosity, the Fofonoff state is a *stable attractor* in the language of dynamical systems theory.

The approximation (2.11) to (2.10) is convenient because integrals like (2.12) are easy to perform only if the argument of exp in (2.10) is at worst a quadratic in the ψ_i. The usual justification for (2.11) is that *discrete* approximations (2.8) typically only conserve E, Q_1, and Q_2. However, this justification is unappealing because it seems to depend on a shortcoming of discrete approximations. A more plausible justification is that (2.11) corresponds to a uniform distribution of probability on the phase-space hypersurface Γ of constant E, Q_1, Q_2. The more exact distribution (2.10) is uniform on a *subset* of Γ, but this subset may sample Γ so densely that (2.12) can be accurately evaluated with (2.11). We regard the numerical experiments in Sections 3 and 4 as a simultaneous test of the validity of the theory leading up to (2.10) and the accuracy of the approximation (2.11).

3. Experiments without forcing or bottom drag

In this section we analyze numerical solutions of (2.1–4) with vanishing wind stress and D a scale-selective eddy viscosity that represents the effects of unresolved small scales by removing the energy that piles up near k_{max}, the highest resolved wavenumber. By the reasoning in Section 2, we expect these solutions to approach steady Fofonoff flow. However, we are here primarily concerned with the *pathway* of approach to the Fofonoff state, which equilibrium statistical mechanics cannot address.

At the small scales on which the eddy viscosity is effective, the dynamics are essentially those of pure two-dimensional turbulence with negligible β. The eddy viscosity in numerical solutions of two-dimensional turbulence is often taken to be of the form

$$D = (-1)^{m+1} \nu (\nabla^2)^m \psi \tag{3.1}$$

where ν is a constant eddy coefficient and m is a positive integer. The choice $m = 1$ mimics the standard molecular friction but does not accurately represent the effect of a sharp cutoff in resolved lengthscales. Larger values of m exacerbate the problem of choosing m coastal boundary conditions (besides no-normal-flow) to go with (3.1). These boundary conditions are as arbitrary as (3.1) itself. However, Marshall (1983) has proposed that the choice of boundary conditions be constrained by the requirement that the eddy viscosity cause no boundary fluxes of Q_1. This is logical because the eddy viscosity operator and associated boundary conditions (which can be combined into a general integro-differential operator) represent the effect of unresolved small scales *within the fluid itself,* and there is no fluid outside the boundaries. However, Marshall's specific suggestion for the case $m = 2$ leads to a boundary flux of E with indefinite sign. Griffa (1988) has shown that this causes unacceptable oscillations of the energy in experiments like those considered here.

To avoid this difficulty, we here use the anticipated vorticity eddy viscosity proposed by Sadourny and Basdevant (1981, 1985), viz.

$$D = D_{AV} \equiv -\nu J(\psi, \nabla^2 J(\psi, \zeta)). \tag{3.2}$$

It can easily be shown that D_{AV} dissipates enstrophy, but not energy or total vorticity, within the body of the fluid, in agreement with the phenomenology of the k^{-3} enstrophy inertial range in two-dimensional turbulence. Moreover, with boundary conditions of no-normal-flow and

$$\frac{\partial}{\partial n} J(\psi, \zeta) = 0 \tag{3.3}$$

(where n denotes the normal direction), D_{AV} causes no boundary fluxes of total vorticity, enstrophy, or energy. Vallis and Hua (1988) report good agreement between (3.2) and the eddy viscosity calculated explicitly from higher resolution experiments.

We now discuss the results of two experiments with eddy viscosity (3.2) and no other forcing or dissipation. The experiments begin from random initial conditions with energy concentrated at nondimensional wavenumbers $k = 3$ to 4 (based upon the basin size L), and (we anticipate) evolve toward steady solutions of (2.13) with γ and y_0 determined by the (conserved) energy

$$E \equiv L^2 U_{rms}^2$$

and total vorticity (2.15). For realistically small initial energy, γ is positive and the final state has a westward interior flow with speed

$$U = \beta/\gamma. \tag{3.4}$$

The boundary layer, of thickness

$$\delta = \sqrt{U/\beta} \tag{3.5}$$

Table 1. Experiments without forcing or bottom drag.

Experiment	QG1	QG2	SM2
Dynamics	quasigeostrophic	quasigeostrophic	stochastic model
Initial Ro	15.9×10^{-3}	2.98×10^{-3}	3.74×10^{-3}
δ (Eq. 3.7)	$3.98\ \Delta x$	$1.30\ \Delta x$	$1.52\ \Delta x$
Z/Z_{abs}	.012	.063	.037
Duration	$81.6\ T_{rms}$	$91.2\ T_{rms}$	$9.48\ T_{rms}$

and velocity magnitude LU/δ, makes the dominant contribution to E. Thus

$$U \approx U_{rms} \sqrt{\delta/L} \tag{3.6}$$

and, combining equations, we find that the boundary layer thickness depends only weakly on the initial energy:

$$\delta \approx Ro^{2/3} L, \tag{3.7}$$

where

$$Ro \equiv \frac{U_{rms}}{\beta L^2} \tag{3.8}$$

is the Rossby number. Eqs. (3.4–8) provide the link between γ and the initial energy.

The latitude y_0 where $\langle \psi \rangle = 0$ is determined by the (conserved) value of the total vorticity Z. If $Z = 0$, then $y_0 = L/2$, and the Fofonoff flow is symmetric about the central latitude. If $Z < 0$ then $y_0 < L/2$ and the northern (anticyclonic) gyre dominates.

Table 1 summarizes the experiments. (The stochastic model experiment SM2 will be discussed in Section 5.) All of our experiments were performed with a resolution of 64 by 64 gridpoints. Finer resolution is impractical because the experiments must run for long times. The coarse resolution puts a lower bound on the initial energy, because the inertial boundary layer thickness (3.7) must be resolved. All of our initial Rossby numbers are small compared to unity, but large compared to realistic ocean values. For example, if $L = 4000$ km and $\beta = 10^{-13}$ cm^{-1} sec^{-1}, then experiment QG1 corresponds to an *rms* velocity U_{rms} of 255 cm sec^{-1}. QG2 corresponds to 47.7 cm sec^{-1}. If finer resolution had permitted smaller initial Rossby numbers, we would expect thinner inertial boundary layers and longer adjustment times, but qualitatively similar behavior to that reported below. Table 1 also gives the boundary layer thickness estimated from (3.7) in units of gridspacing Δx; the normalized total vorticity Z/Z_{abs}, where

$$Z_{abs} \equiv \iint_A |\zeta|\, dx\, dy; \tag{3.9}$$

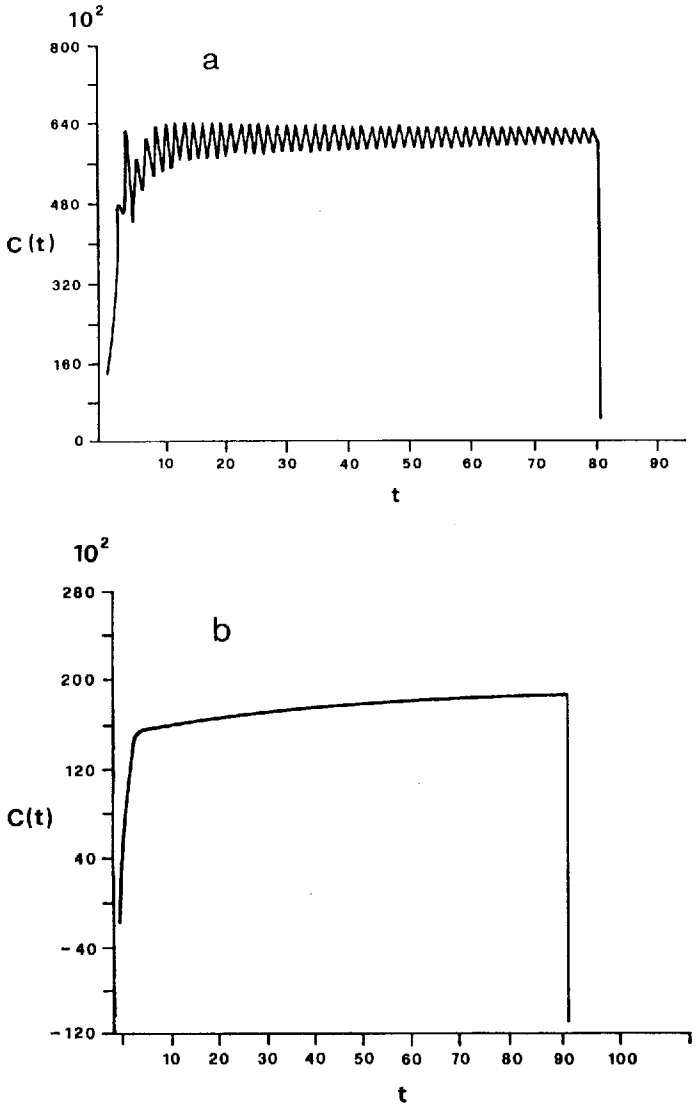

Figure 1. Anticorrelation $C(t)$, defined by (2.18), between the relative vorticity and latitude (in arbitrary units) versus time (in units of turnover time T_{rms}) in the free quasigeostrophic experiments (a) QG1 and (b) QG2; and (c) in the stochastic model experiment SM2. The increase in $C(t)$ with time is an indication of the emergence of Fofonoff flow.

and the duration of each experiment in units of the turn-over time,

$$T_{rms} \equiv L/U_{rms}. \tag{3.10}$$

The Jacobian in (2.1) is computed using the Arakawa scheme, which conserves discrete analogues of E, Q_1, and Q_2. In all of our experiments the eddy coefficient ν has

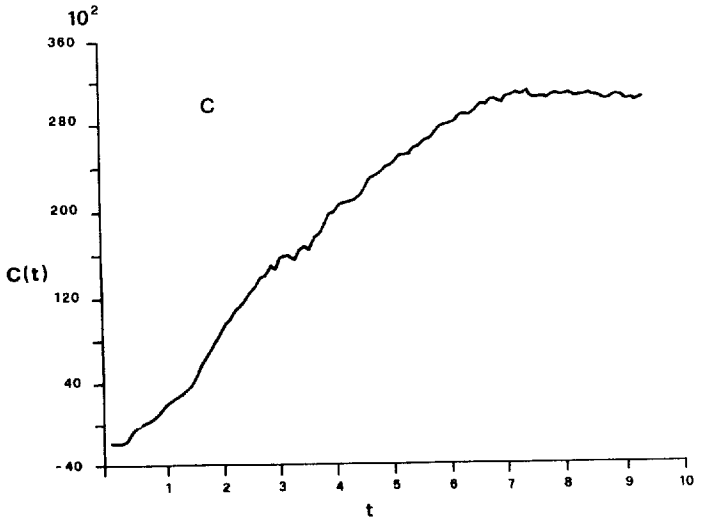

Figure 1. (Continued)

the minimum value needed to prevent a noticeable pileup of energy at scales comparable to Δx.

All of the experiments reported in this paper were run for very long times, of the order of 10^5 time-steps. Such long runs are required, because Rossby waves impose a relatively short time-step on the calculation and also inhibit the nonlinear interactions between modes.

a. Experiment QG1. Figure 1a shows the evolution of the anticorrelation $C(t)$, defined by (2.18), between vorticity and latitude in experiment QG1. The increase of $C(t)$ from its near-zero initial value is an indication of the emergence of Fofonoff flow. As shown in Figure 1a, $C(t)$ increases rapidly until time 4.5 T_{rms}, indicating a rapid accumulation of positive (negative) vorticity in the southern (northern) half of the basin. The much slower *average* increase in $C(t)$ after 4.5 T_{rms} is marked by gradually decaying oscillations. As explained below, these oscillations are caused by basin-scale Rossby waves that die out very slowly. The average fractional increase in $C(t)$ over the last 60 T_{rms} is only 4.4×10^{-4}.

Figures 2 and 3 show snapshots of the streamfunction and the relative vorticity during the initial phase of rapid adjustment. During the first 2 T_{rms}, the reflection properties of Rossby waves rapidly increase the energy and enstrophy near the western boundary. Fluid particles moving rapidly along the western boundary then carry negative vorticity northward and positive vorticity southward. This mechanism for the segregation of vorticity, which leads to the formation of two oppositely rotating gyres, was recognized by Veronis (1970). By time 3 T_{rms} the fluid particles and the inertial boundary layers they set up have reached the eastern boundary, and by 4 T_{rms} the

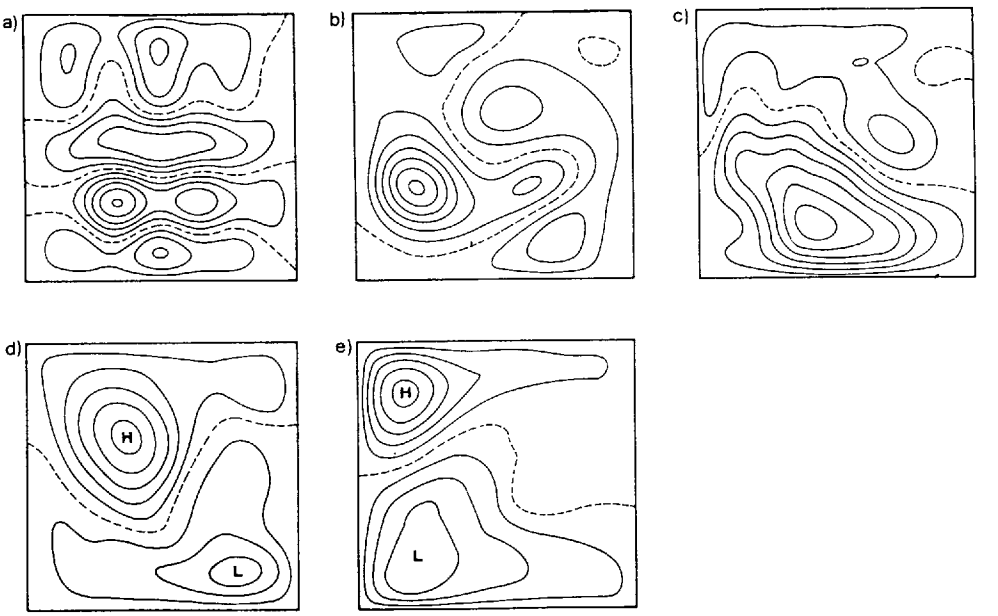

Figure 2. Streamfunction at times separated by T_{rms}, from the beginning of free quasigeostrophic experiment QG1. The flow is rapidly adjusting to the Fofonoff state, although significant east/west asymmetry is still evident at 4 T_{rms}.

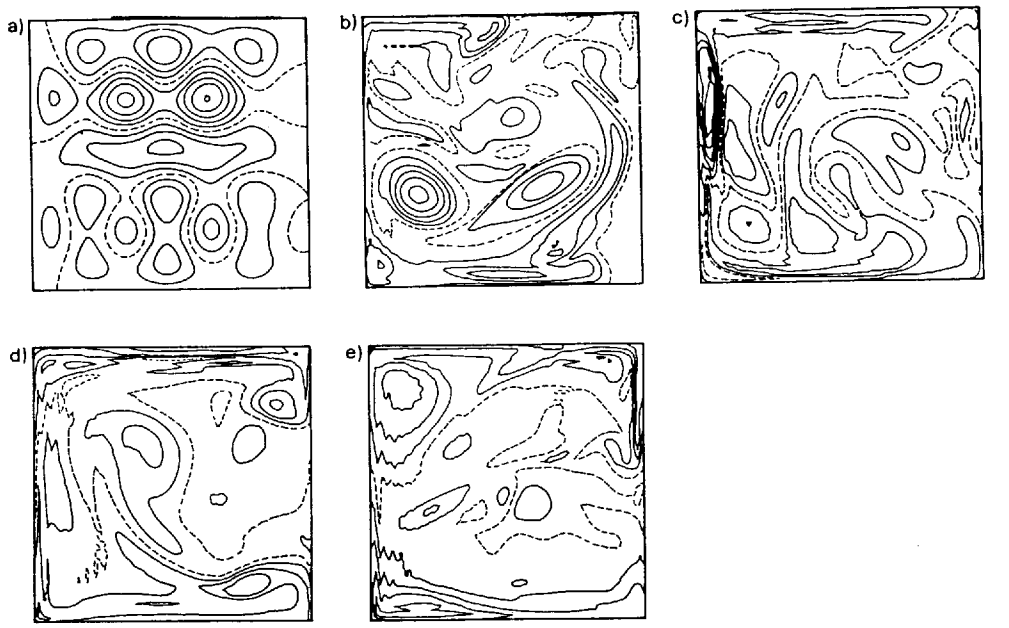

Figure 3. Relative vorticity at times separated by T_{rms}, from the beginning of experiment QG1. The adjustment to the Fofonoff state is characterized by an accumulation of large relative vorticity along the northern and southern boundaries.

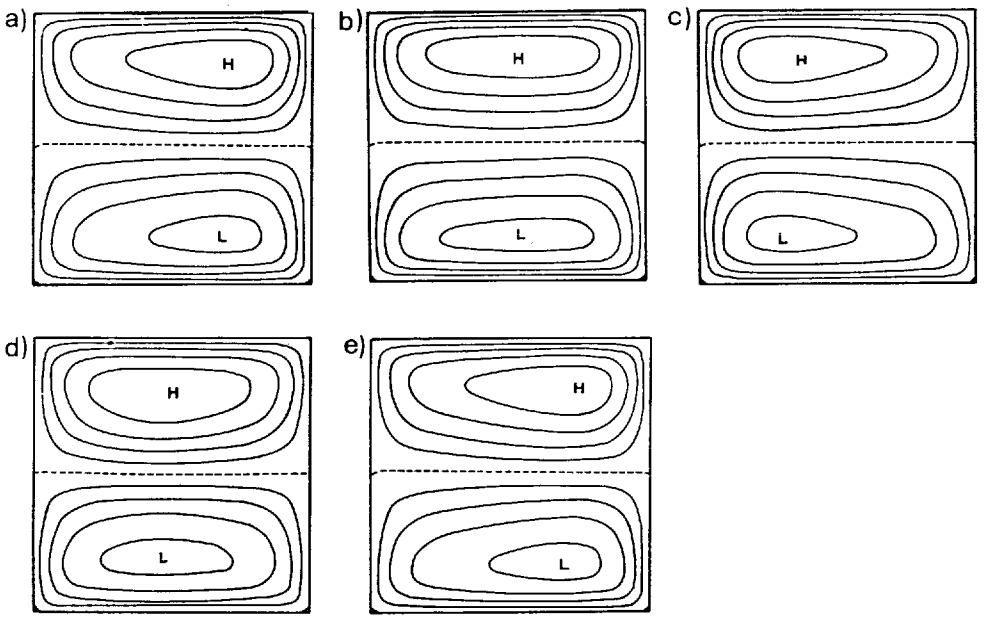

Figure 4. Streamfunction during one Rossby wave period beginning at time 78 T_{rms} in experiment QG1. The time interval between pictures is .4 T_{rms}.

extension and energy of the eastern inertial boundary layers are comparable to those in the west.

It follows from (2.1) and (2.18) that (neglecting eddy viscosity)

$$\frac{dC(t)}{dt} = \left[\frac{1}{2}\beta \int_0^L |\nabla\psi|^2 \, dy\right]_{x=L}^{x=0}. \tag{3.11}$$

Thus the emerging east-west symmetry is directly associated with the leveling-off of $C(t)$. Holloway (1986a) reports unpublished numerical experiments in which the emergence of Fofonoff flow coincides with the growth of $C(t)$.

By time 20 T_{rms} fluctuations on the grid scale Δx have been dissipated by the eddy viscosity. The remaining oscillations are apparently basin-scale Rossby waves whose predicted frequency

$$\omega_{nm} = \frac{\beta L}{2\pi\sqrt{n^2 + m^2}} \tag{3.12}$$

agrees well with that observed in Figure 1a for $(n, m) = (1, 2)$. These Rossby waves are excited when the system apparently "overshoots" its adjustment toward Fofonoff flow early in the experiment; the maximum *instantaneous* value of $C(t)$ is actually attained near the end of the initial phase of rapid adjustment. Figure 4 shows the time evolution of ψ during one oscillation period at 78 T_{rms}.

The streamfunction and potential vorticity averaged over the last 20 T_{rms} of QG1 are shown in Figure 5a. The boundary layer thickness in Figure 5a agrees well with the estimate given in Table 1. A more sensitive comparison between the final state of QG1 and Fofonoff flow is provided by Figure 6a, which is a scatter plot of $\langle q \rangle$ and $\langle \psi \rangle$ for the same averaging period. Figure 6a supports the prediction of (2.13) that $\langle q \rangle$ be a linear function of $\langle \psi \rangle$ in the final Fofonoff state, but it also shows that the slope $d\langle q \rangle / d\langle \psi \rangle$ differs significantly between the two gyres. This difference in slope decreases slowly throughout the experiment, from a difference of 45% between gyres at time 13.5 T_{rms} to a difference of 31% at time 78.5 T_{rms}. The near-constancy of the slope within each gyre suggests that the two gyres adjust rapidly to separate quasiequilibrium states, which then interact slowly to bring about the final global equilibrium.[3]

By (2.14), the slope $\gamma = d\langle q \rangle / d\langle \psi \rangle$ is a function of the "inverse temperatures" λ_i. Thus the slowly equilibrating gyres are closely analogous to two bodies with high heat conductivities that are separated by a poorly-conducting wall. Although the two bodies eventually have the same temperature, they pass through a sequence of states with different but uniform temperatures.

b. Experiment QG2. In comparison to QG1, experiment QG2 has a much smaller initial energy and a slightly larger average total vorticity (refer again to Table 1). We find that QG2 also evolves toward Fofonoff flow, but after an initial period of rapid adjustment, this evolution proceeds much more slowly than in the more energetic experiment QG1.

In QG2, inertial gyres form near the northern and southern boundaries within the first few T_{rms}. These gyres have initial latitudinal widths of about $L/4$, but are visible only in time-averages between the times 4.5 T_{rms} and 28 T_{rms}. The interior region outside the gyres is dominated by Rossby waves. Between about 5 T_{rms} and the end of the experiment, the gyres slowly expand to a latitudinal width of $L/3$.[4] By the end of QG2, the two-gyre pattern is evident also in snapshots, but even time-averages (Fig. 5b) do not yet closely resemble Fofonoff flow. The asymmetry between the northern and southern gyres in Figure 5b is a consequence of the positive total vorticity in the initial conditions. At the end of QG2 $\langle q \rangle$ depends quasilinearly on $\langle \psi \rangle$ within each of the gyres (Fig. 6b). In the region between the gyres $\langle \psi \rangle \approx 0$.

As shown in Figure 1b, the anticorrelation $C(t)$ in QG2 increases rapidly until the time 4.5 T_{rms} at which the inertial gyres reach the eastern boundary, but, in contrast to QG1, $C(t)$ also increases steadily thereafter, indicating that QG2 never reaches its equilibrium state. The fractional change in $C(t)$ over the last 60 T_{rms} of QG2 is 2.6×10^{-3}. Experiment QG2 also shows less evidence of basin-scale Rossby waves (compare

3. G. F. Carnevale (personal communication) reports a similar phenomenon in numerical experiments on quasigeostrophic flow over topography.

4. William R. Young (personal communication) had previously noticed inward growth of inertial gyres from latitudinal boundaries.

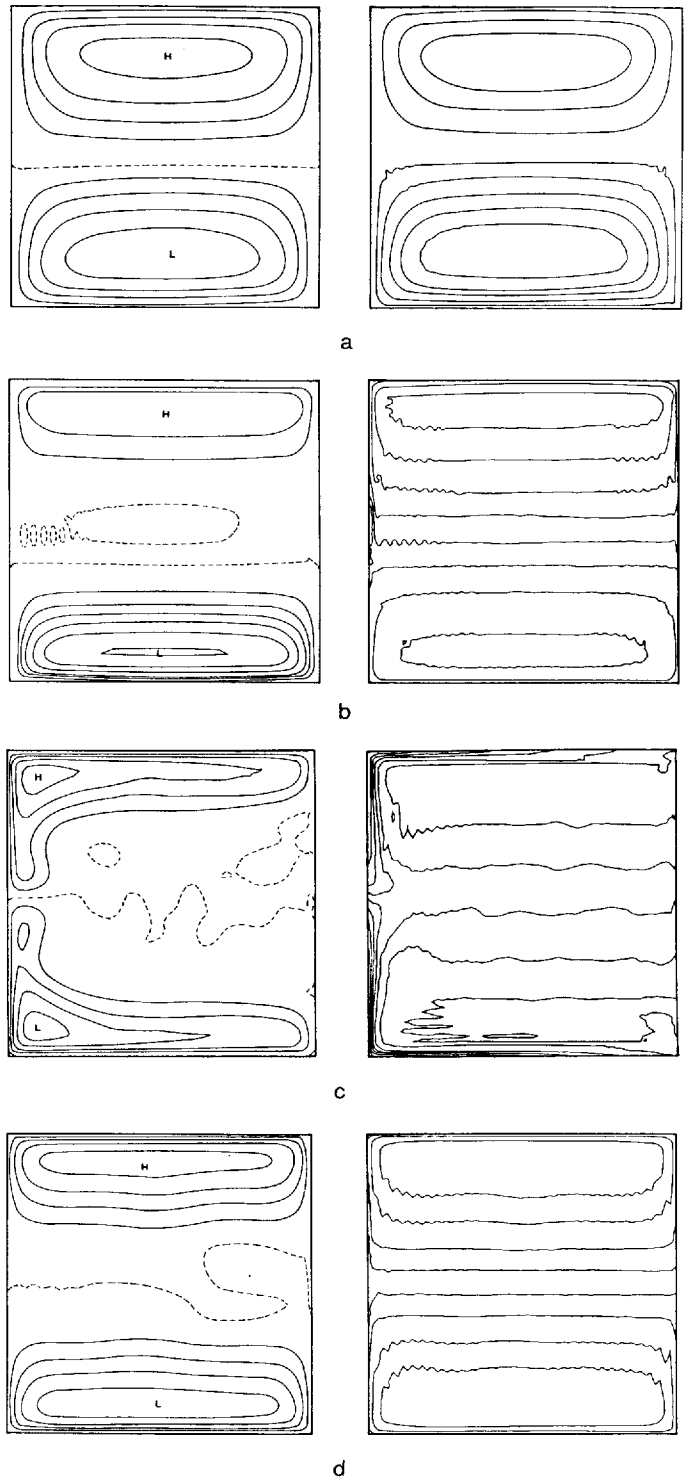

Figure 5. Average streamfunction (left) and potential vorticity (right) near the end of free experiments (a) QG1; (b) QG2; (c) SM2; and (d) the instantaneous streamfunction and potential vorticity at the end of wind-driven experiment QGa. Only QG1 closely resembles Fofonoff flow, but QG2 and SM2 seem to be evolving toward it. The wind in QGa is compatible with Fofonoff flow, and the average circulation therefore resembles that in QG2.

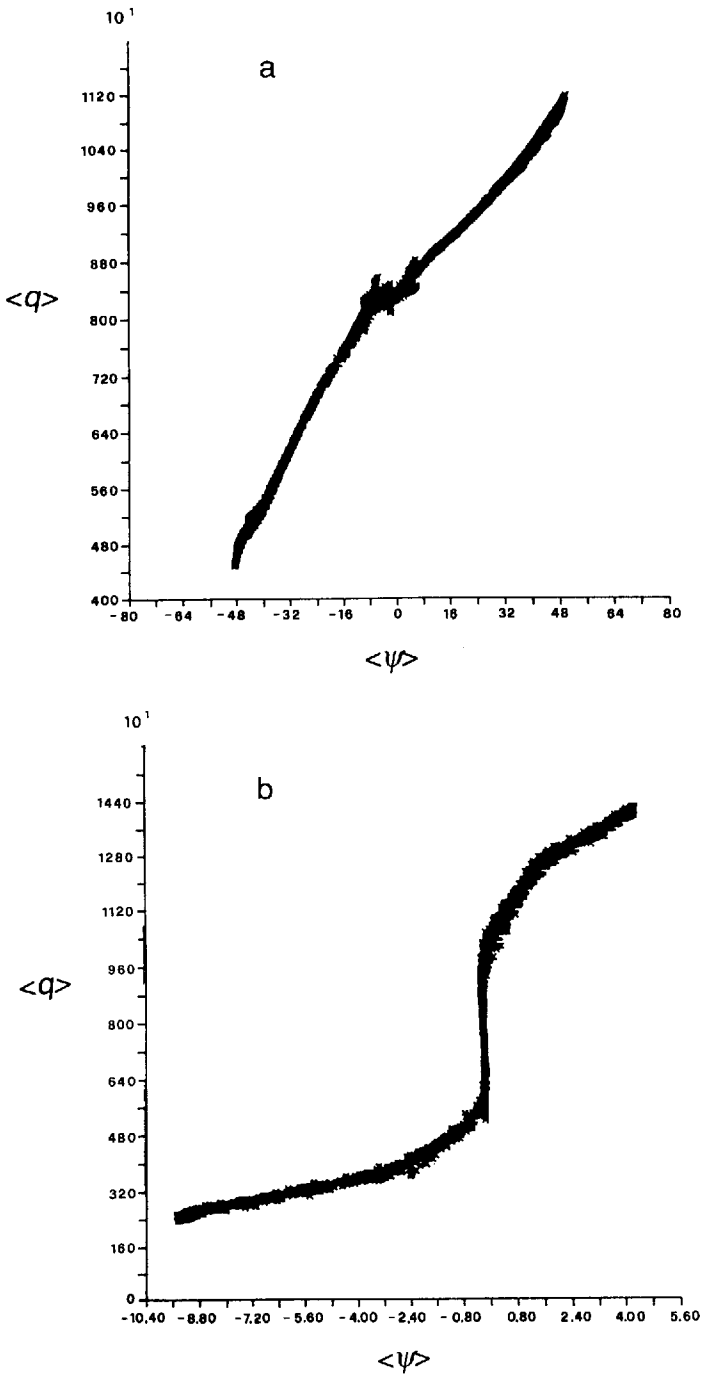

Figure 6. Scatter plot of $\langle q \rangle$ versus $\langle \psi \rangle$ near the end of: free quasigeostrophic experiments (a) QG1; (b) QG2; wind-driven quasigeostrophic experiments (c) QGa; (d) QGb; (e) QGc1; (f) QGc2; and wind-driven stochastic model experiments (g) SMb; and (h) SMc2. Statistical mechanics predicts a linear relation between $\langle q \rangle$ and $\langle \psi \rangle$.

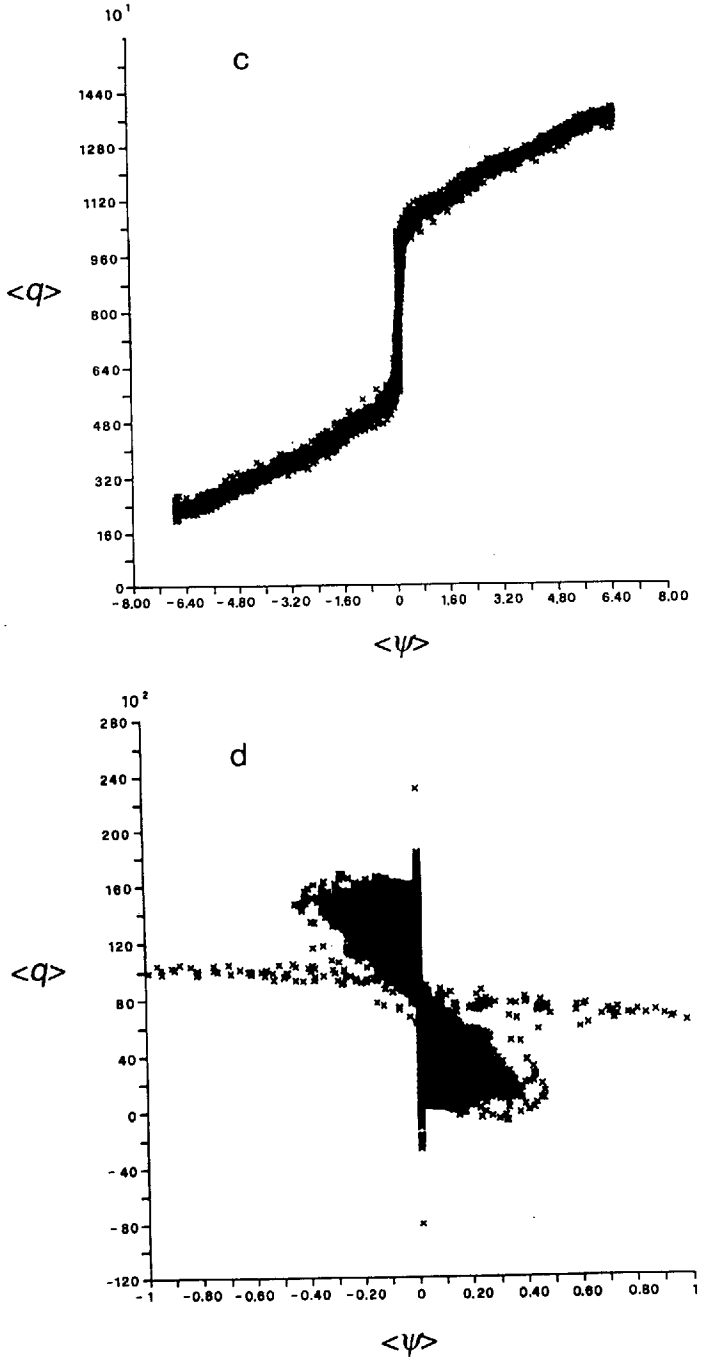

Figure 6. (Continued)

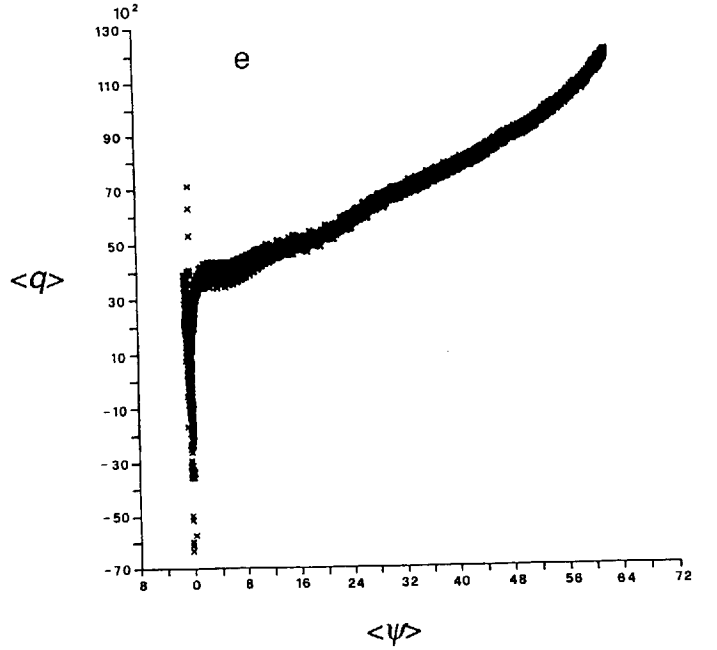

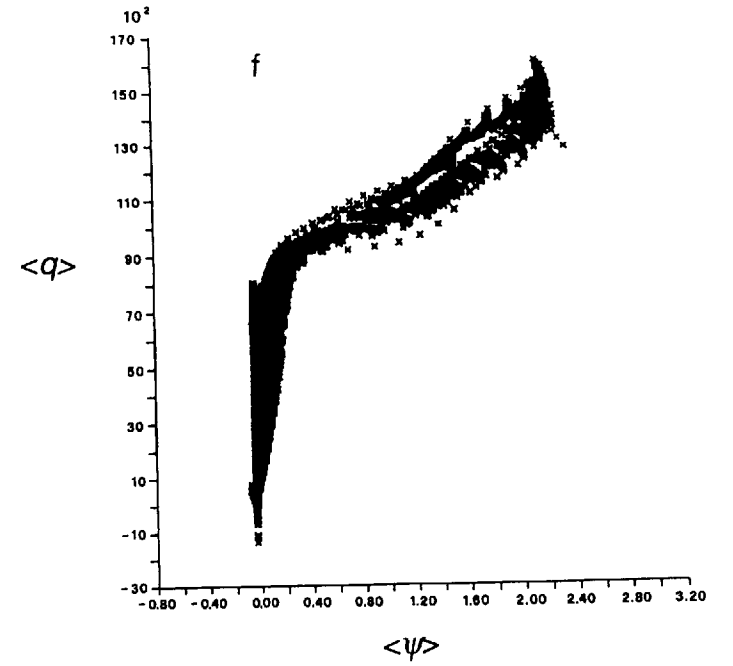

Figure 6. (Continued)

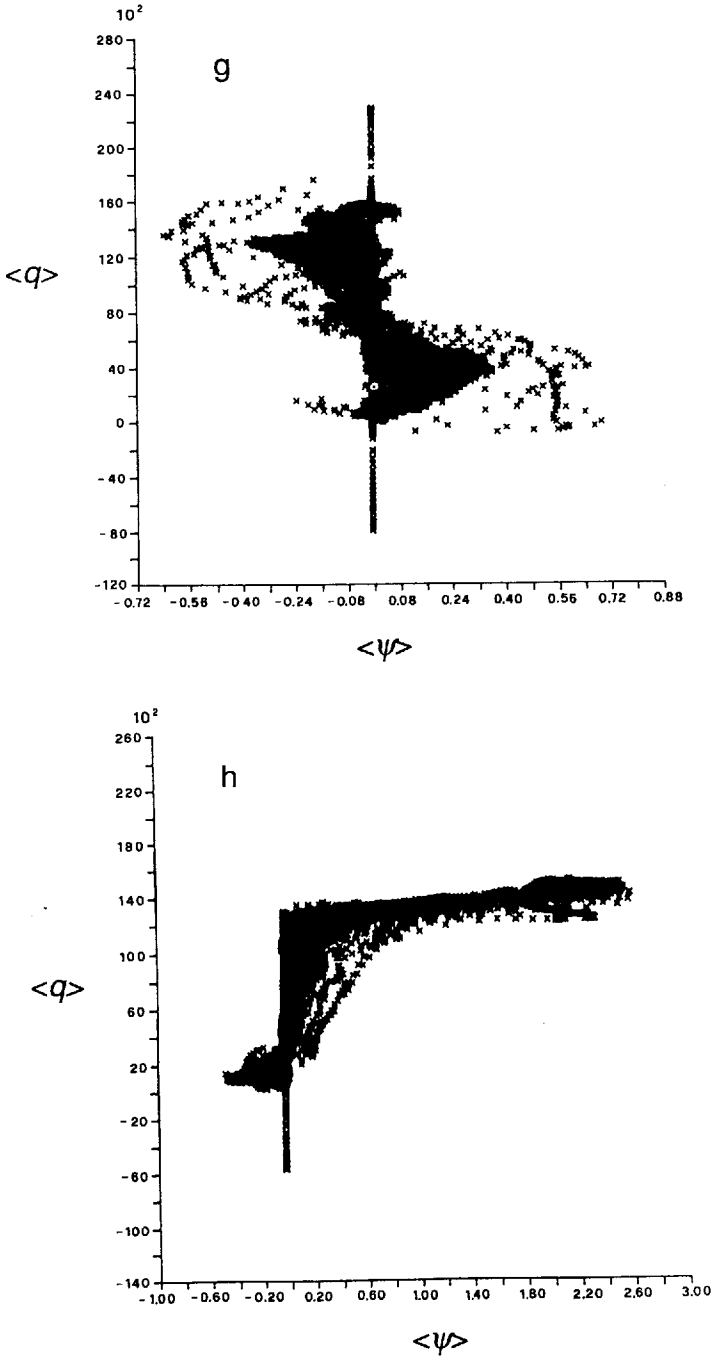

Figure 6. (Continued)

Figs. 1a–b) than did QG1. This too is apparently because of its "quieter" (i.e. less energetic) start.

As shown in Table 1, the thinner inertial boundary layer in QG2 is much more poorly resolved than in QG1. This is the reason for the small-amplitude gridpoint oscillations in Figure 5b.

The smaller initial latitudinal width and subsequent slow expansion of the gyres in experiment QG2 is possibly explained by Rhines' (1975) suggestion that nonlinear interactions are inhibited on lengthscales at which the Rossby wave frequency (3.12) exceeds the "advection frequency"

$$U_{rms}\left\{\left(\frac{n\pi}{L}\right)^2+\left(\frac{m\pi}{L}\right)^2\right\}^{1/2}, \tag{3.13}$$

where U_{rms} is a reasonable estimate of the velocity inside the inertial gyres. We find that the ratio of (3.12) to (3.13) is approximately unity when $(n, m) = (1, 4)$. The corresponding ratio in QG1 is only about $\frac{1}{5}$.

In both QG1 and QG2, the small-scale fluctuations are rapidly removed by the eddy viscosity, and the remaining time-dependent motions seem to be primarily basin-scale Rossby waves. These disappear slowly, and in the less energetic experiment QG2 seem to slow the adjustment to Fofonoff flow. In both experiments the gyres form initially on a timescale of a few T_{rms} but the complete adjustment to the final Fofonoff state requires many T_{rms}. In the following section we introduce forcing and a bottom-drag friction with a decay time scale between T_{rms} and the long time required to reach the exact Fofonoff state. We therefore anticipate that the role of nonlinear interactions in these forced experiments will be to move the system toward states like the ones observed in QG1 and QG2 after the initial phase of rapid adjustment.

4. Experiments with forcing and bottom drag

In this section we analyze numerical solutions of (2.1–4) with nonzero wind stress, and dissipation operator

$$D = D_{AV} - \epsilon\zeta \tag{4.1}$$

equal to the eddy viscosity (3.2) plus a bottom drag with drag coefficient ϵ. All of our experiments use the wind stress $\tau(x, y) = (\tau(y), 0)$ with one of the following choices for $\tau(y)$, $0 < y < L$:

$$\tau(y) = -\sin(\pi y/L) \equiv \tau_a(y) \tag{4.2a}$$

$$\tau(y) = +\sin(\pi y/L) \equiv \tau_b(y) \tag{4.2b}$$

$$\tau(y) = -\cos(\pi y/L) \equiv \tau_c(y) \tag{4.2c}$$

corresponding, respectively, to (a) an easterly wind with a maximum at $y = L/2$; (b) a westerly wind with a maximum at $y = L/2$; and (c) easterlies on $y < L/2$ and westerlies

on $y > L/2$. Cases (a) and (b) correspond, in the linear limit, to two counter-rotating Sverdrup gyres. Case (c) corresponds to the classical single subtropical gyre.

The dramatic differences in the numerical solutions corresponding to the various wind fields (4.2) can be anticipated from the time-average of (2.1–4), viz.

$$\nabla \cdot (\langle \mathbf{u} \rangle \langle q \rangle) + \nabla \cdot (\mathbf{u}'q') = \left(\frac{\tau_0}{\rho H}\right) \operatorname{curl} \boldsymbol{\tau} - \epsilon \langle \zeta \rangle. \tag{4.3}$$

Here, primes denote departures from the time-average, and the eddy viscosity (whose effect on the time-average flow is expected to be small) has been ignored. The integral of (4.3) over the area enclosed by a mean streamline $\langle \psi \rangle$ = constant, yields

$$\oint \langle \mathbf{u}'q' \rangle \cdot \mathbf{n}\, dr = \left(\frac{\tau_0}{\rho H}\right) \oint \boldsymbol{\tau} \cdot d\mathbf{r} - \epsilon \oint \langle \mathbf{u} \rangle \cdot d\mathbf{r} \tag{4.4}$$

where $d\mathbf{r}$ is the counterclockwise displacement around the mean stream line and $\mathbf{n}$ is the outward unit normal.

By the reasoning above, nonlinear interactions always drive the system toward *quasi-steady* Fofonoff flow. If the Fofonoff state were actually reached, then (4.4) would have to be satisfied, on every closed streamline, with the left-hand side set equal to zero. Thus, if the two terms on the right-hand side of (4.4) cannot balance when $\langle \mathbf{u} \rangle$ is the mean velocity in the hypothetical Fofonoff state, then the nonlinear terms cannot succeed in pushing the wind-driven system very close to the Fofonoff state, and we say that the wind is incompatible with Fofonoff flow. The wind may be incompatible with Fofonoff flow over all or only over a part of the ocean basin.

If the wind is incompatible with Fofonoff flow, we find that the two terms on the right-hand side of (4.4) generally have opposite signs (as expected from the fact that (1.3) must be positive), but the mean flow $\langle \mathbf{u} \rangle$ is much smaller than in cases where the wind is compatible with Fofonoff flow. The Reynolds flux of potential vorticity (i.e. the left-hand side of (4.4)) must therefore be important, and we do indeed observe large temporal fluctuations in such cases.

Table 2 summarizes the forced quasigeostrophic experiments. (The stochastic model experiments SMb and SMc2 will be discussed in Section 5.) In the identifier for each experiment, the letter a, b, or c refers to the wind stress in (4.2). The first two columns in Table 2 give the wind stress magnitude τ_0 and decay coefficient ϵ in nondimensional form. If $\beta = 10^{-13}$ cm^{-1} sec^{-1}, $H = 4000$ m, and $L = 4000$ km (for example), then the values in Table 2 correspond to wind stresses of 1.0 and 2.0 dyne cm^{-2}. The corresponding drag decay time

$$T_\epsilon \equiv \epsilon^{-1} \tag{4.5}$$

would be 2.54 and 12.7 years. Table 2 also gives the Rossby number (3.8) and the ratio of the advection time (3.10) to the drag time (4.5) at the end of each experiment, and the duration of each experiment in drag times. We remark that none of the

Table 2. Experiments with forcing and bottom drag.

Experiment	$\pi\tau_0/(\rho H\beta^2 L^3)$ (10^{-5})	$\epsilon/\beta L$ (10^{-4})	Final Ro (10^{-3})	T_{rms}/T_ϵ	Duration (T_ϵ)
QGa	2.45	3.13	2.69	.12	1.6
QGb	2.45	3.13	.63	.50	1.7
QGc1	1.23	.625	14.7	.0043	2.9
QGc2	1.23	3.13	.94	.33	5.6
SMb	2.45	3.13	.78	.40	1.1
SMc2	1.23	3.13	.89	.35	1.8

experiments reach an exactly steady statistical state. All of the experiments except QGc2 were run with 64 by 64 gridpoints; QGc2 required 128 by 128 gridpoints to resolve the inertial boundary layer. All of the experiments except QGc1 begin from random initial conditions; QGc1 begins from a state of rest. Of course, the initial conditions of these dissipative experiments should eventually become irrelevant.

a. Double-gyre experiments QGa and QGb. Experiments QGa and QGb differ by only a minus sign in the wind stress, but QGa, in which the wind blows in the same direction as interior Fofonoff flow, is compatible with Fofonoff flow, whereas QGb is not. As anticipated by the foregoing remarks, the equilibrium state of QGa resembles steady Fofonoff flow, while the equilibrium state of QGb is very unsteady, with a very small mean velocity. These two experiments thus nicely demonstrate the folly of attempting to predict the behavior of the system from a scaling analysis alone.

In QGa a symmetric two-gyre mean flow emerges by time .4 T_ϵ. The energy in the gyres builds up steadily until the end of the experiment, although the latitudinal extent of each gyre does not increase much from the value of $L/4$ attained early in the experiment. The inertial boundary layer thicknesses agree well with estimates based on (3.5) using the velocity in the interior of the gyres. The final flow in QGa (Fig. 5d) differs only slightly from its time-average. Figure 6c gives the scatter plot of $\langle q \rangle$ and $\langle \psi \rangle$ averaged over the last .35 T_ϵ of QGa. The resemblance between QGa and QG2 (which had about the same Rossby number) is obvious.

An analysis of the balance of terms in the time-average of (2.1) for experiment QGa shows that $J(\langle \psi \rangle, \langle q \rangle)$ balances $\beta \partial \langle \psi \rangle / \partial x$ in the eastern and western inertial boundary layers, whereas the former balances the bottom drag in the northern and southern boundary layers. The region between the gyres has a Sverdrup balance not obvious in Figure 5d.

Experiment QGb differs from QGa only in that its wind field is reversed, and now opposes interior Fofonoff flow. However, by the end of QGb the energy has reached a constant average value much lower (by a factor of 20) than the final energy in QGa (which is still increasing).

In QGb, a two-gyre mean flow also emerges by time .4 T_ϵ, but it consists of narrow

gyres closely confined to the western boundary. At first these mean gyres are concentrated near $y = L/2$. As time increases, the gyres expand to reach the northwestern and southwestern corners of the basin, but two intense recirculation cells remain near $y = L/2$.

Figure 7a shows snapshots of the streamfunction and potential vorticity at the end of experiment QGb. Only the recirculation cells near $(x, y) = (0, L/2)$ are visible in the instantaneous fields. The instantaneous flow is dominated by fluctuations in which Rossby waves with wavenumbers $(n, m) = (3, 2)$ and $(4, 2)$ are evident.

Figure 7c shows the streamfunction and potential vorticity averaged over the last .5 T_ϵ of experiment QGb. The weak mean flow shows little resemblance to Fofonoff flow. An analysis of the balance of terms in the averaged potential vorticity equation (2.1) shows that the recirculating cells are maintained by Reynolds transport of potential vorticity. The basin interior has a weak Sverdup balance.

The scatter plot of $\langle q \rangle$ and $\langle \psi \rangle$ is shown in Figure 6d. The differences from all previous experiments are dramatic. The points corresponding to locations outside the small recirculating gyres are spread over a finite area of the $\langle \psi \rangle - \langle q \rangle$ plane. The nearly horizontal line of constant $\langle q \rangle$, which corresponds to points within the two small recirculating gyres, was also noted by Marshall (1984). The vertical line of zero $\langle \psi \rangle$ corresponds to points on the boundary.

Experiments QGa and QGb tend to confirm our interpretation that the nonlinear terms in (2.1) drive the flow toward the Fofonoff state along the same phase-space pathway followed by the unforced, undamped experiments reported in Section 3. In the case QGa in which the wind blows in the same direction as Fofonoff flow, the flow approaches a state which is very similar to the final state of experiment QG2. The final state of QG2, although differing significantly from Fofonoff flow, seems to be converging toward it. However, it is likely that QGa, although its energy is still increasing, will remain stuck on the way to the Fofonoff state, because the drag time T_ϵ is very small compared to the long time apparently needed to reach the Fofonoff state at this Rossby number.

In experiment QGb, the westerly wind tries to build up an eastward interior mean flow, but the nonlinear terms, which want to push the system toward the Fofonoff state, disrupt it. In consequence, the mean flow is in the general direction of the wind but is very weak (except in the two small recirculation gyres near the western boundary).

b. Single-gyre experiments QGc1 and QGc2. In experiments QGc1 and QGc2, the wind has the classical subtropical gyre pattern (4.2c) of trade winds on $y < L/2$ and westerlies on $y > L/2$. The wind stress has only half the amplitude of the wind stress in experiments QGa and QGb, but it now exerts a nonzero (negative) net torque on the fluid. Since this wind stress is compatible with a Fofonoff flow in which the eastward return flow occurs predominately along the northern boundary, we expect a resemblance between these solutions and the thermal equilibrium states.

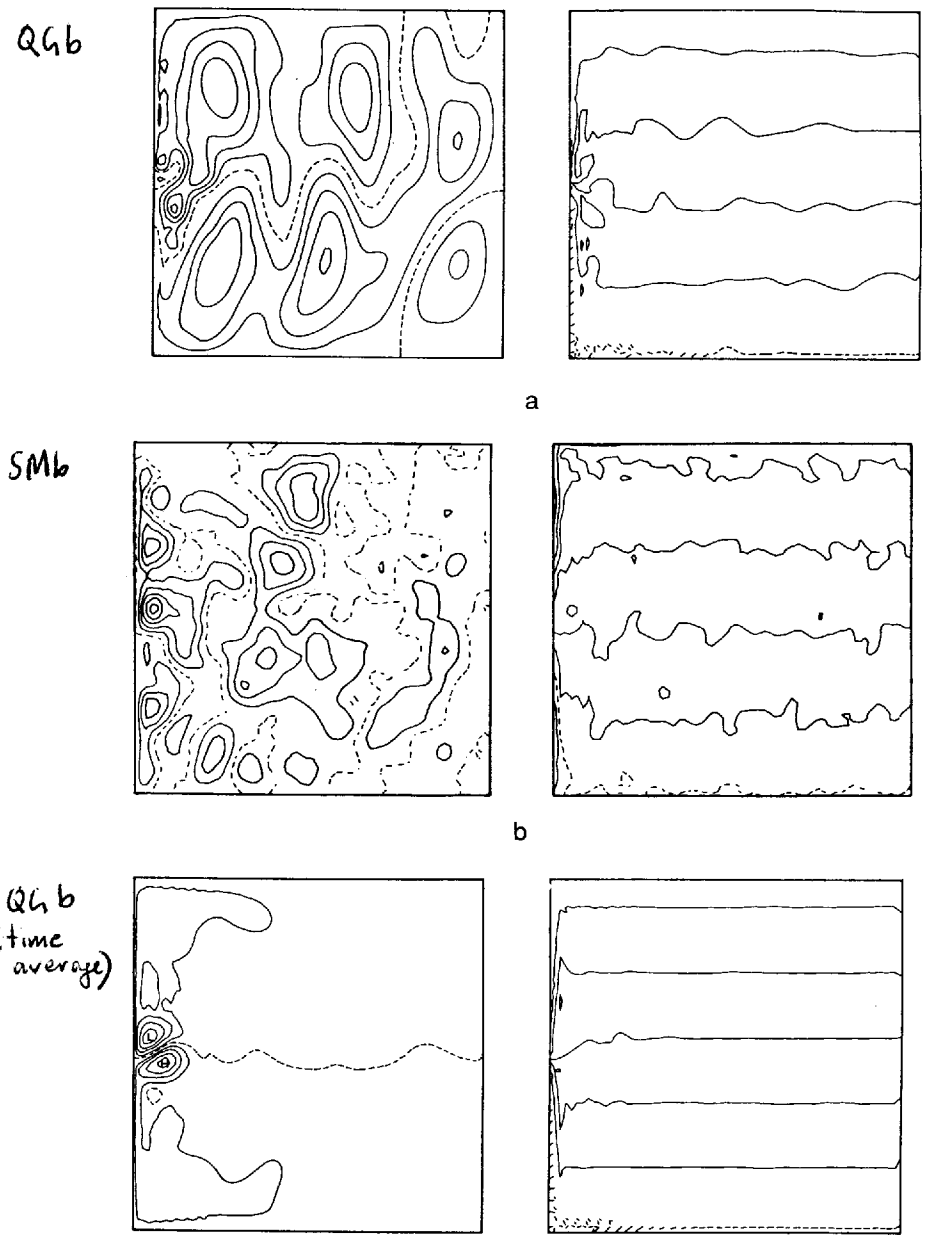

Figure 7. The instantaneous streamfunction (left) and potential vorticity (right) at the end of wind-driven quasigeostrophic experiment (a) QGb; and corresponding stochastic model experiment (b) SMb; and the time-average streamfunction and potential vorticity near the end of these same experiments, (c) QGb; and (d) SMb. The wind in these experiments is not compatible with Fofonoff flow.

$$\tau_0 = \sin\left(\frac{\pi y}{L}\right)$$

SMb (time average)

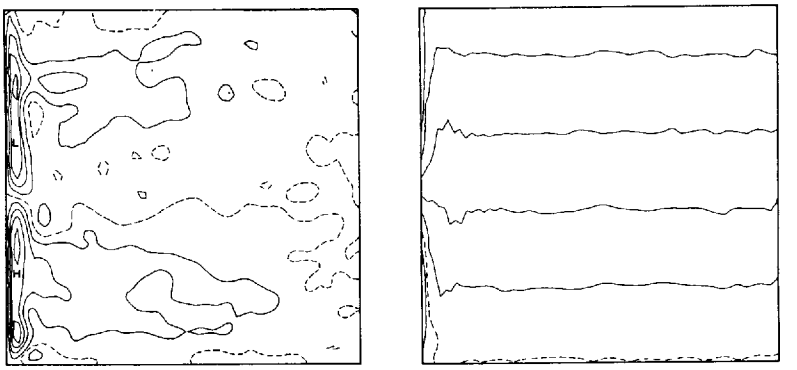

d

Figure 7. (Continued)

Experiments QGc1 and QGc2 differ only in the bottom-drag coefficient ϵ. The bottom drag in experiment QGc2 is the same as in all other experiments, but the drag in QGc1 is five times smaller, and the final Rossby number is therefore much larger in QGc1. Refer again to Table 2.

For given wind stress, the equilibrium total vorticity (2.15) can be predicted from the time- and basin-average of (2.1), viz.

$$\left(\frac{\tau_0}{\rho H}\right) \iint_A \text{curl}\, \tau \, dx \, dy = \epsilon \langle Z \rangle. \tag{4.6}$$

A comparison between the measured total vorticity and that predicted by (4.6) provides one measure of nearness to statistical equilibrium. By the end of the experiments, the total vorticities in experiments QGc1 and QGc2 were within 3% of the values predicted by (4.6). The energy in QGc1 was still increasing, but showed signs of leveling off. The energy in QGc2 had attained a nearly constant value.

In QGc1 a small anticyclonic eddy appears in the northwest corner of the basin by time .04 T_ϵ. The eddy expands along the northern boundary to the northeast corner. The resulting gyre then expands slowly southward. By time .32 T_ϵ it covers 80% of the basin, and thereafter ceases expanding. However, its strength and boundary layer thicknesses keep increasing until the end of the experiment.

Figure 8a shows snapshots of the streamfunction and potential vorticity at the end of QGc1. These snapshots closely resemble the time-averages. The southern 20% of the basin is an eddy region in which the weak mean flow is cyclonic despite the fact that the wind torque is everywhere negative.

Analysis of the time-average potential vorticity equation shows that the inertial boundary layers in QGc1 have the same balances as in QGa. The quasi-steady interior of the gyre shows a weak Sverdrup balance. In the southern eddy region, the convergence of Reynolds vorticity flux balances the bottom torque.

QG c1

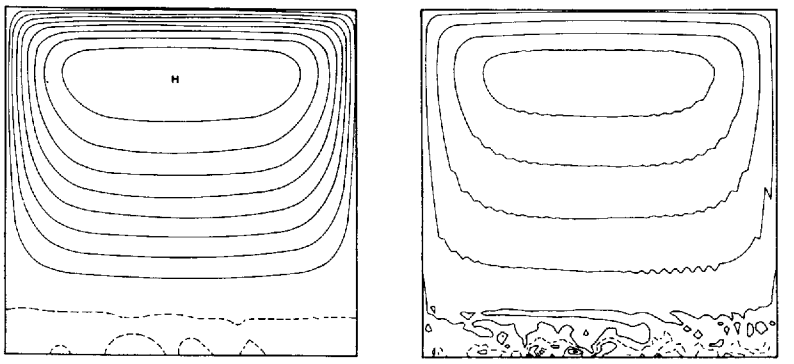

a

QG c2

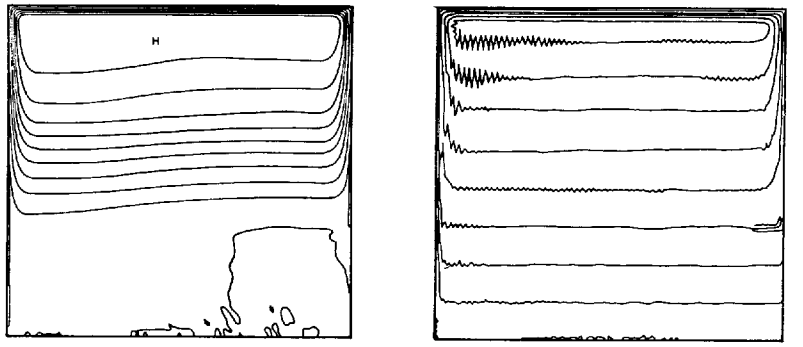

b

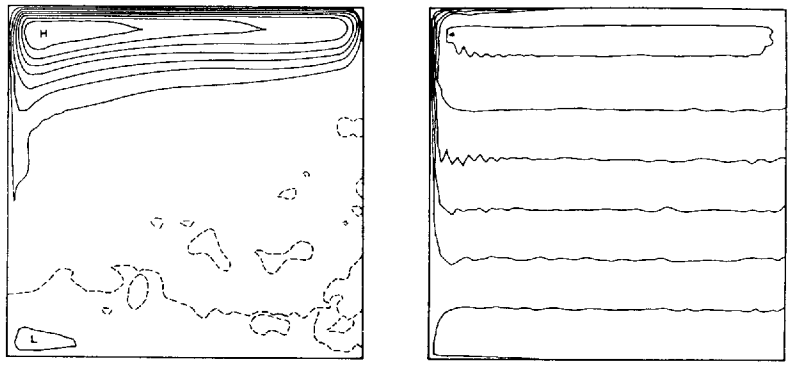

c

Figure 8. Instantaneous streamfunction and potential vorticity at the end of wind-driven quasigeostrophic experiments (a) QGc1 and (b) QGc2; and (c) the time-average streamfunction near the end of stochastic model experiment SMc2, which corresponds to QGc2. The wind in these experiments corresponds to the classical subtropical gyre, and is generally compatible with Fofonoff flow.

Figure 6e shows the scatter plot of $\langle q \rangle$ and $\langle \psi \rangle$ for QGc1. As in QGa, $\langle q \rangle$ depends linearly on $\langle \psi \rangle$ throughout the gyre; the mean streamfunction $\langle \psi \rangle$ is very small in the southern eddy region.

Experiment QGc2 has the same forcing but a much larger bottom drag than QGc1. In QGc2 the inertial gyre covers only about 60% of the basin, and the final flow (Fig. 8b) shows a greater east/west asymmetry. Because the inertial flow is weaker, the Sverdrup balance is more evident in Figure 8b. Again, the weak mean flow in the southern eddy region is maintained by eddy transports. The scatter plot of $\langle q \rangle$ and $\langle \psi \rangle$ for QGc2 (Fig. 6f) is qualitatively similar to that for QGc1, but the linear relationship between $\langle q \rangle$ and $\langle \psi \rangle$ within the inertial gyre is somewhat less sharp.

Our interpretation that the nonlinear terms drive the system toward the Fofonoff state seems also to provide a qualitative explanation for experiments QGc1 and QGc2. The new feature of these latter two experiments is the uniformly negative sign of the wind torque. The total vorticity must then be negative by (4.6). A negative average vorticity Z corresponds to a Fofonoff flow in which $y_0 < L/2$ in (2.13) so that the northern anticyclonic gyre dominates. However, Z is apparently not so negative that $y_0 < 0$; that is, the target Fofonoff state also has a southern cyclonic gyre on $0 < y < y_0$. Since the wind stress in experiments QGc exerts a negative torque *throughout* the flow, the two terms on the right-hand side of (4.4) cannot balance one another around closed streamlines within a southern Fofonoff gyre. In the southern region, the Reynolds flux of potential vorticity (i.e. the left-hand side of (4.4)) must be important. The southern eddy region in experiment QGc is therefore like the entire flow in QGb, where the wind everywhere opposes Fofonoff flow.

5. Stochastic model experiments

The previous results suggest that the integral conservation laws (on which the equilibrium statistical mechanics is solely based) largely define the role of the nonlinear terms in (2.1). In this section we test this idea by comparing solutions of (2.1–4) to solutions of the stochastic model equation

$$\nabla^2 \psi_t + J(\psi, \zeta^*) + \beta \psi_x = \left(\frac{\tau_0}{\rho H}\right) \operatorname{curl} \tau + D \tag{5.1}$$

where ζ^* is a random variable with only gross statistical properties in common with ζ. The boundary condition remains $\psi = 0$. Eqs. (2.1) and (5.1) differ only in that $\zeta^* = \nabla^2 \psi^*$ replaces ζ in the Jacobian term *only*. When $\tau = D = 0$, (5.1) automatically conserves the energy E and total vorticity Z (or Q_1). If we agree to constrain the choice of ζ^* by

$$\iint_A qJ(\psi, \zeta^* + \beta y)\, dx\, dy = 0 \tag{5.2}$$

then (5.1) also conserves the potential enstrophy Q_2, and the thermal equilibrium states